High-pressure phases of group-II difluorides: Polymorphism and superionicity

Joseph R. Nelson,[1,*] Richard J. Needs,[1] and Chris J. Pickard[2,3]

[1]*Theory of Condensed Matter Group, Cavendish Laboratory, J. J. Thomson Avenue, Cambridge CB3 0HE, United Kingdom*

[2]*Department of Materials Science and Metallurgy, University of Cambridge, 27 Charles Babbage Road, Cambridge CB3 0FS, United Kingdom*

[3]*Advanced Institute for Materials Research, Tohoku University, 2-1-1 Katahira, Aoba, Sendai, 980-8577, Japan*

(Received 6 October 2016; published 21 February 2017)

We investigate the high-pressure behavior of beryllium, magnesium, and calcium difluorides using *ab initio* random structure searching and density functional theory (DFT) calculations, over the pressure range 0–70 GPa. Beryllium fluoride exhibits extensive polymorphism at low pressures, and we find two new phases for this compound—the silica moganite and $CaCl_2$ structures—which are stable over the wide pressure range 12–57 GPa. For magnesium fluoride, our searching results show that the orthorhombic "O-I" TiO_2 structure ($Pbca$, $Z = 8$) is stable for this compound between 40 and 44 GPa. Our searches find no new phases at the static-lattice level for calcium difluoride between 0 and 70 GPa; however, a phase with $P\bar{6}2m$ symmetry is close to stability over this pressure range, and our calculations predict that this phase is stabilized at high temperature. The $P\bar{6}2m$ structure exhibits an unstable phonon mode at large volumes which may signal a transition to a superionic state at high temperatures. The group-II difluorides are isoelectronic to a number of other AB_2-type compounds such as SiO_2 and TiO_2, and we discuss our results in light of these similarities.

DOI: 10.1103/PhysRevB.95.054118

I. INTRODUCTION

The group-II difluorides form materials with a wide variety of technological uses. BeF_2, and mixtures of it with further fluorides and difluorides, are used to create glasses for use in infrared photonics, which have excellent transmittance in the UV. BeF_2 glass itself has a large band gap of 13.8 eV [1,2]. BeF_2 is chemically stable and is employed as a mixture component in nuclear reactor molten salts, where it is useful as a coolant, and is also capable of dissolving fissile materials [3]. MgF_2 is birefringent with a wide wavelength transmission range, and is used in the manufacture of optical components such as polarizers [4]. CaF_2 also offers a high transmittance across a wide range of wavelengths and is used in optical systems, as well as an internal pressure standard [5,6]. MgF_2 and CaF_2 occur naturally as the minerals sellaite and fluorite; therefore, high pressure modifications of these compounds are of interest in geophysics.

Group-II difluorides have 16 valence electrons per formula unit, and are isoelectronic to other AB_2 compounds of industrial or geophysical significance, such as TiO_2 and SiO_2. As such, these compounds share many similar crystal structures, albeit stable at different pressures. Because of this structural similarity, group-II difluorides have been investigated as structural analogs of silica phases [7]. BeF_2 is particularly similar to silica at low pressures [8], as in addition to being isoelectronic, the fluoride (F^-) and oxide (O^{2-}) ions have similar radii and polarizabilities, and the Be/F and Si/O atomic radii ratios are similar at $\approx$0.3 [9]. MgF_2 has also been explored as a model for higher pressure silica phases [10].

We are interested in the structures and phases of Be-, Mg-, and CaF_2 at ambient and elevated pressures, and the implications of such phases for other AB_2 compounds. Our approach to determining stable phases in these compounds uses computational structure searching alongside density functional theory (DFT) calculations, and we elect to explore the pressure range 0–70 GPa.

II. METHODS

The *ab initio* random structure searching (AIRSS) technique [11] is used to search for group-II difluoride structures at three pressures: 15, 30, and 60 GPa. AIRSS is a stochastic method which generates structures randomly with a given number of formula units. A minimum atom-atom separation is specified for the generated structures, e.g., we set the Be-Be, Be-F, and F-F minimum separations for the case of BeF_2. These separations are chosen based on short AIRSS runs. We can also impose symmetry constraints on our generated structures such that low symmetry structures are not considered. This strategy tends to speed up the searches because such low-symmetry structures are unlikely to have low energies according to Pauling's principle [12,13], although we allocate part of our searching time to check low symmetry structures, for completeness. AIRSS has a proven track record of predicting structures in a diverse variety of systems that have subsequently been verified by experiment, such as in compressed silane, aluminium hydride, high-pressure hydrogen sulfide, and xenon oxides [14–17].

We limit our searches to a maximum of eight formula units (24 atoms) per cell. In addition to AIRSS, we supplement our searches with a set of 15 known AB_2-type structures taken from a variety of compounds; see the Supplemental Material [18] for a full list of these structures. Structures generated by AIRSS or taken from known AB_2 compounds are relaxed to an enthalpy minimum using a variable-cell geometry optimization calculation. For this, we use density-functional theory (DFT) as implemented in the CASTEP plane-wave pseudopotential code [19], with internally generated ultrasoft pseudopotentials [20] and the Perdew-Burke-Ernzerhof (PBE) exchange-correlation functional [21]. Our DFT calculations

*jn336@cam.ac.uk

use a 800 eV plane-wave basis set cutoff, and a Brillouin zone sampling density of at least $2\pi \times 0.04$ Å^{-1}. Our calculations of phonon frequencies use the quasiharmonic approximation (QHA) [22,23] and a finite-displacement supercell method, as implemented in CASTEP.

As well as searches for new BeF_2, MgF_2, and CaF_2 structures, we have also carried out variable stoichiometry structure searching at 60 GPa, to examine the possibility of other thermodynamically stable compositions. These searches predict that BeF_2 and MgF_2 are the only stable stoichiometries at 60 GPa, while both CaF_2 and CaF_3 are stable at that pressure. Our predicted CaF_3 structure is cubic with $Pm\bar{3}n$ symmetry, and the same structure has in fact been previously predicted for high-pressure aluminium hydride (AlH_3) [15]. We have not examined the properties of high-pressure CaF_3 further, and in what follows we focus only on the AB_2 difluoride stoichiometry. Convex hulls for our variable stoichiometry searches are given in the Supplemental Material [18].

Semilocal density functionals such as PBE typically underestimate the calculated band gap in materials. In order to capture the optical properties of the group II difluorides, we perform optical band gap calculations with the nonlocal Heyd-Scuseria-Ernzerhof (HSE06) functional [24]. This functional incorporates 25% screened exchange and is expected to generally improve the accuracy of band gap calculations carried out with DFT, though at a greater computational cost. We adopt the following calculation strategy: structures are first relaxed with the PBE functional, norm-conserving pseudopotentials [25], a basis set cutoff of 1600 eV and a relatively sparse Brillouin zone sampling of $2\pi \times 0.1$ Å^{-1}. The HSE06 functional is then used with PBE-relaxed geometries for a self-consistent calculation of the electronic bands of the structure. Our stress calculations indicate that the use of the HSE06 functional with PBE geometries gives rise to small forces of $\lesssim$0.1 eV/Å on each atom. Electronic density of states calculations are then performed using the OPTADOS code [26–28]. Additional information on the electronic structure calculations in this study can be found in the Supplemental Material [18].

III. BERYLLIUM DIFLUORIDE

A. Low-pressure results

Beryllium fluoride has several thermodynamically accessible phases which have been obtained in experimental studies. At temperatures below its melting point (820 K) and pressures at or below atmospheric pressure, the α-quartz, β-quartz, α-cristobalite, β-cristobalite, and glass phases of BeF_2 have been prepared under various conditions [29,30].

Our results from structure searching calculations at low pressures (0–8 GPa) are summarized in Fig. 1(a), which shows the static-lattice enthalpies of several BeF_2 structures as a function of pressure. Beryllium fluoride shows extensive polymorphism at low pressures; we find at least 10 structures for BeF_2 [all those shown in Fig. 1(a), except coesite-I and coesite-II] lying within about 20 meV/f.u. of one another at 0 GPa. The α- and β-quartz, and α- and β-cristobalite structures are part of this set of 10 structures. Within our current calculational framework (DFT-PBE), the α-cristobalite structure is lowest in enthalpy at 0 GPa, lying 8.9 meV/f.u. below α-quartz, but other low enthalpy structures are also of interest as they can be stabilised by temperature. There is some experimental evidence for as-yet-unknown high-temperature low-pressure BeF_2 phases [31], and metastable structures produced in our searches provide useful reference crystal structures that could be matched to available experimental data at elevated temperatures. We remark here that the PBE functional may not provide a completely accurate energy ordering for these structures at low pressure. For example, in silica, DFT-PBE also predicts that the α-cristobalite structure has a lower enthalpy than the α-quartz structure at 0 GPa. However, high pressure phase transition pressures in silica calculated with PBE are in excellent agreement with accurate quantum Monte Carlo calculations [32].

A recent study by Rakitin *et al.* found a $C2/c$ structure for BeF_2 which is close in enthalpy to α-quartz at 0 GPa [33]. Results using AIRSS produce five further polymorphs for BeF_2, labeled "Moganite," $P2_12_12_1$-I, $P2_12_12_1$-II, $C2/c-4\times2$, and $P2_1/c$ in Fig. 1(a), which have static-lattice enthalpies of +0.9, +0.4, −8.9, −4.9, and −0.3 meV/f.u. relative to the α-quartz phase at 0 GPa. We discuss each of these in more detail below.

Moganite. The "Moganite" polymorph, which turned up in our searches (and was also included in our set of 15 AB_2 structures [18]), is BeF_2 in the silica moganite structure with Si → Be and O → F. This has space group $C2/c$ and six formula units of BeF_2 in the primitive cell.

$P2_12_12_1$-II. At the pressures shown in Fig. 1(a), the $P2_12_12_1$-II polymorph has space group symmetry $P4_32_12$ (no. 96), and is actually an enantiomer of α-cristobalite. A mirror-image transformation $(x,y,z) \rightarrow (-y,-x,z)$, i.e., a reflection of atomic positions in the (110) plane, relates the two structures. This situation is entirely analogous to SiO_2, where rigid-unit phonon modes (RUMs) distort the β-cristobalite structure to one of either $P4_12_12$ symmetry (our α-cristobalite) or to $P4_32_12$ symmetry (our $P2_12_12_1$-II). Coh *et al.* [34] employ the notation $\tilde{\alpha}_1$ and $\tilde{\alpha}_1'$ respectively for these two cristobalite structures. Enthalpy-pressure curves for the α-cristobalite and $P2_12_12_1$-II structures lie on top of one another in Fig. 1(a), and our calculations give the overall change in enthalpy going from β-cristobalite to $\tilde{\alpha}_1$ or $\tilde{\alpha}_1'$ as −21.2 meV/BeF_2; the equivalent quantity is −34.4 meV/SiO_2 in silica. Above 11 GPa, the $P2_12_12_1$-II structure distorts to the lower space group symmetry $P2_12_12_1$ (no. 19), and the enthalpy curves for it and the α-cristobalite structure start to diverge [Fig. 1(b)].

Open framework structures. The $P2_12_12_1$-I, $C2/c$–4×2, and $P2_1/c$ structures in Fig. 1(a) are low-density polymorphs which are previously unreported in BeF_2. The notation "$C2/c$–4×2" refers to the fact that this structure is a low-pressure variant of the "$P2_1/c$ ($Z=8$), 4×2-type" structure shown in Fig. 1(c). Our DFT − PBE calculations show that these polymorphs are energetically relevant in silica, where they lie 5.5, 15.7, and 5.9 meV/SiO_2 in energy below α-quartz at 0 GPa, which suggests them as likely silica polymorphs as well. The monoclinic angle in the $P2_1/c$ structure is close to 90°; hence we also investigate a higher symmetry version of this structure with $Pnma$ symmetry, whose enthalpy is found to be 2.2 meV/SiO_2 below α-quartz [this structure is not

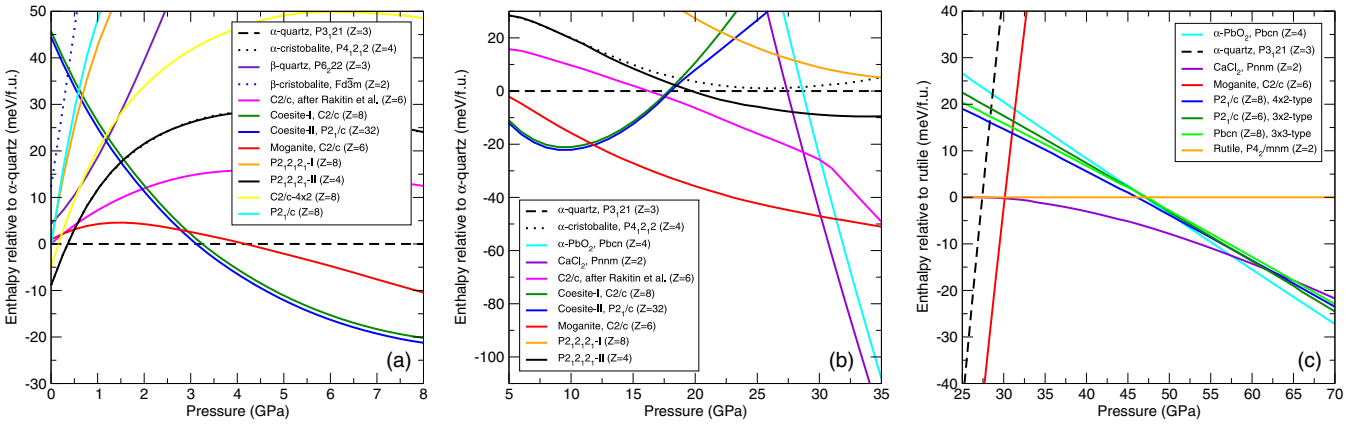

FIG. 1. Static lattice enthalpies for BeF_2 calculated with the PBE functional over the pressure ranges (a) 0–8 GPa, (b) 5–35 GPa, and (c) 25–70 GPa. In (a) and (b), enthalpies are shown relative to the α-quartz phase, while in (c) they are shown relative to the rutile phase.

shown in Fig. 1(a)]. Calculated lattice parameters and atomic positions for these structures are provided as Supplemental Material [18].

We query the ICSD [35] and International Zeolite Association (IZA) [36] databases to check if these four structures are already known in SiO_2. Our $C2/c$–4×2 structure matches no. 75654 in the ICSD, which is "Structure 8" in the simulated annealing structure prediction work of Boisen *et al.* [37], after the latter is relaxed using DFT. However, we find no matching SiO_2 structures in these databases for our $P2_12_12_1$-I, $P2_1/c$, and $Pnma$ structures. Analysis of these three structures using the TOPOS code [38] shows that they are all of the same topological type as the ABW zeolite. They have framework densities of 18.9, 18.6, and 18.5 Si/1000 Å^3 (cf. α-quartz, with 24.9 Si/1000 Å^3), while the ABW silica structure itself is slightly less dense at 17.6 Si/1000 Å^3, with an enthalpy 3.9 meV/SiO_2 above α-quartz. While BeF_2 and SiO_2 share many chemical similarities (as mentioned in Sec. I), the Be-F bond is much weaker than the Si-O bond, resulting in a lower melting point and hardness for BeF_2 [29]. Nevertheless, our results show that BeF_2 also supports open framework zeolitelike structures, and highlights the utility of searching for potential zeolite structures in model systems such as BeF_2. The large number of polymorphs we encounter lying close to one another in energy suggest BeF_2 as a potential tetrahedral framework material.

B. High-pressure results

Our structure searching calculations show that the application of pressure (0.4 GPa) favors the α-quartz phase, as seen in Fig. 1(a). Between 3.1 and 3.3 GPa, the silica "coesite-I" or "coesite-II" structure [39] with $Z = 8$ or 32 then becomes the lowest-enthalpy structure for BeF_2. We find that over the pressure range 0–18 GPa, the coesite-I and II structures are nearly identical. The coesite-II structure is close to a supercell of coesite-I, but the atomic positions in coesite-II deviate slightly from those expected for a perfect supercell, and the coesite-II structure lies consistently about 1 meV/BeF_2 below coesite-I over this pressure range. The coesite-I phase has been found in experimental studies on BeF_2, at 3 GPa and $\approx$1100 K [31]. Previous work [33] reported that a new structure of $C2/c$ symmetry then becomes stable between 18 and 27 GPa; our calculations instead show that BeF_2 is most stable in the silica moganite structure, which also has $C2/c$ symmetry, between 11.6 and 30.1 GPa [see Fig. 1(b)]. Above 30.1 GPa, we find that the orthorhombic $CaCl_2$ structure with space group $Pnnm$ becomes stable [Fig. 1(b)], eventually giving way to the denser α–PbO_2 structure above 57.5 GPa [Fig. 1(c)]. The moganite and $CaCl_2$ structures are depicted in Fig. 2.

The enthalpy-pressure curve for the $CaCl_2$ structure emerges smoothly from that for the rutile structure (space group $P4_2/mnm$), which is also the case in silica, where a ferroelastic phase transition occurs between these two structures near 50 GPa [40]. For BeF_2 at the static lattice level, our calculations exclude the stability of the rutile structure over the pressure range 0–70 GPa, though we note that this phase lies only a fraction of a meV per BeF_2 higher in enthalpy than the $CaCl_2$ phase at 30.1 GPa, as seen in Fig. 1(c). Earlier studies [33,41] have already examined a number of the structures discussed here; however, the stability of BeF_2 in the moganite and $CaCl_2$ structures is new, and according to our calculations dominates the high-pressure phases of BeF_2 over the pressure range 11.6–57.5 GPa.

Figure 1(c) shows a band of three enthalpy-pressure curves, labeled $Pbcn$ ($Z = 8$), $P2_1/c$ ($Z = 6$), and $P2_1/c$ ($Z = 8$), whose energy lies in close proximity to the α–PbO_2 curve. These three structures emerged from our searches and have a similar, but slightly lower density than the α–PbO_2 phase for BeF_2. They are close to stability at 60 GPa, but are not predicted to be stable over the pressure range 0–70 GPa. We identify these phases as members of the class of silica polymorphs introduced by Teter *et al.* [42], which are a set of structures described as intermediaries to the $CaCl_2$ and α–PbO_2 silica phases. Our $Pbcn$ ($Z = 8$) and $P2_1/c$ ($Z = 6$) structures correspond to the "3×3" and "3×2" structure types, while our $P2_1/c$ ($Z = 8$) structure is not explicitly discussed in Ref. [42] and would be referred to as "4×2" type. We will encounter these phases again in our results for MgF_2.

Summary. To briefly summarize our search results for BeF_2, we predict the following series of pressure-induced phase

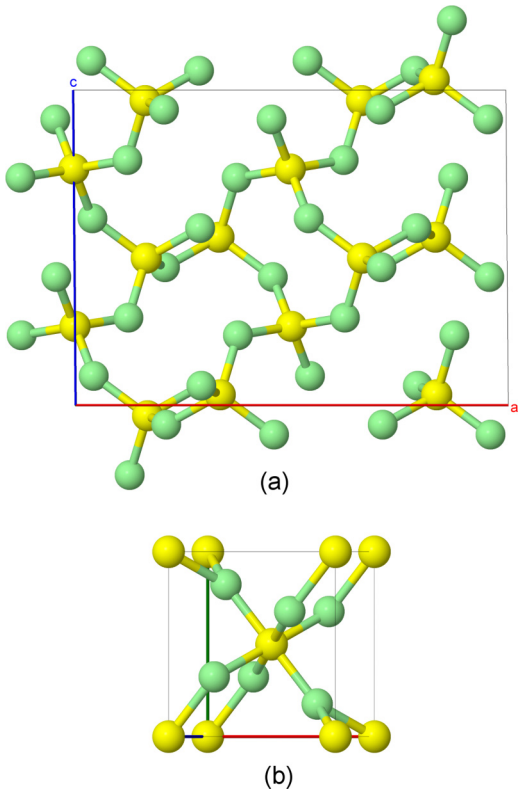

FIG. 2. (a) BeF_2 in the $C2/c$ moganite phase at 20 GPa with fourfold coordinated Be atoms, viewed down the b (and in this case, monoclinic) axis. The lattice a and c axes point horizontal and almost vertical in the page, respectively. (b) BeF_2 in the $Pnnm$ $CaCl_2$ phase at 50 GPa, with sixfold coordinated Be atoms. Beryllium atoms in yellow, fluorine atoms in green. Lattice parameters and atomic positions for these structures are given as Supplemental Material [18].

transitions at the static-lattice level:

$$\alpha\text{-cristobalite}\ (P4_12_12) \xrightarrow{0.4\ \text{GPa}} \alpha\text{-quartz}\ (P3_121) \xrightarrow{3.1/3.3\ \text{GPa}} \text{coesite-I/II}\ (C2/c)$$
$$\xrightarrow{11.6\ \text{GPa}} \text{moganite}\ (C2/c) \xrightarrow{30.1\ \text{GPa}} CaCl_2\ (Pnnm) \xrightarrow{57.5\ \text{GPa}} \alpha\text{-}PbO_2\ (Pbcn),$$

with the labeled arrows showing the calculated transition pressures. Our searches also demonstrate numerous metastable polymorphs for BeF_2.

C. Optical band gaps in BeF_2

As mentioned in Sec. I, BeF_2 has a large band gap at ambient pressure and is used in a number of optical applications. We examine the optical band gap in BeF_2 as a function of pressure, with the results shown in Fig. 3. The optical gap is found to be tunable, increasing by around 0.06 eV/GPa over the pressure range 0–70 GPa. We expect BeF_2 to therefore maintain its high UV transmittance with increasing pressure, with potentially useful high pressure applications. The electronic density of states (DOS) of the moganite and $CaCl_2$ phases are also given as Supplemental Material [18].

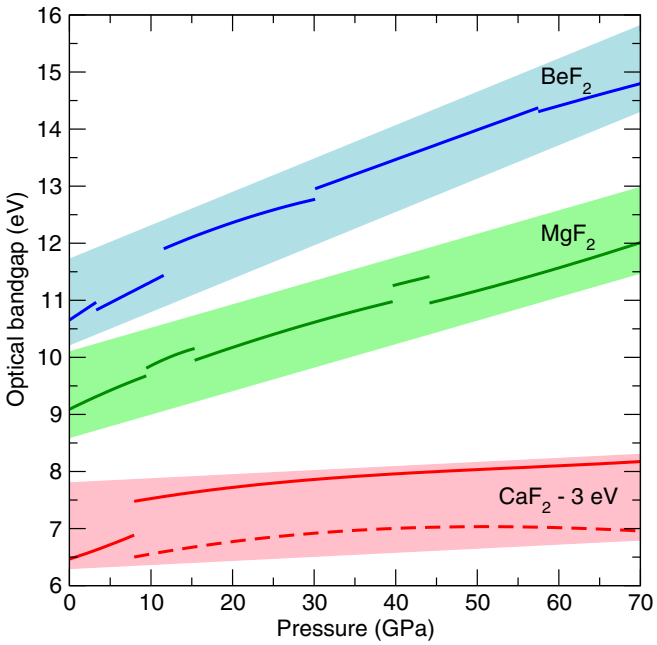

FIG. 3. Optical band gaps in Be-, Mg-, and CaF_2 as calculated using the HSE06 functional, over the pressure range 0–70 GPa. For visibility, the band gaps in CaF_2 have been shifted down by 3 eV. Discontinuities in the solid curves are due to phase transitions between different structures, while the shaded regions serve to guide the eye. The dashed curve in CaF_2 corresponds to the $P\bar{6}2m$ phase, which is not stable at the static lattice level but which we predict is stabilized by temperature.

IV. MAGNESIUM DIFLUORIDE

MgF_2 adopts the rutile $P4_2/mnm$ structure at room temperature and pressure. X-ray diffraction experiments indicate a transformation to the $CaCl_2$ structure at 9.1 GPa, then to a pyrite structure with space group $Pa3$ and $Z = 4$ near 14 GPa, and have also recovered a mixture of α–PbO_2 and rutile MgF_2 upon decompression [10]. DFT calculations, including those of the present study, actually show that the $CaCl_2$ structure is never stable for MgF_2 and instead predict the α–PbO_2 structure to have a window of stability between 10 and 15 GPa, with the $CaCl_2$ structure slightly higher in enthalpy.

The results from our structure searches are given in Fig. 4. Based on our static-lattice results, we predict the following sequence of stable structures and phase transitions with rising pressure:

$$\text{rutile}\ (P4_2/mnm) \xrightarrow{9.4\ \text{GPa}} \alpha\text{-}PbO_2\ (Pbcn) \xrightarrow{15.4\ \text{GPa}} \text{pyrite}\ (Pa3) \xrightarrow{39.6\ \text{GPa}} \text{O-I}\ (Pbca)$$
$$\xrightarrow{44.1\ \text{GPa}} \text{cotunnite}\ (Pnma).$$

Previous theoretical studies [43,44] have already considered the rutile, α–PbO_2, pyrite, and cotunnite phases of

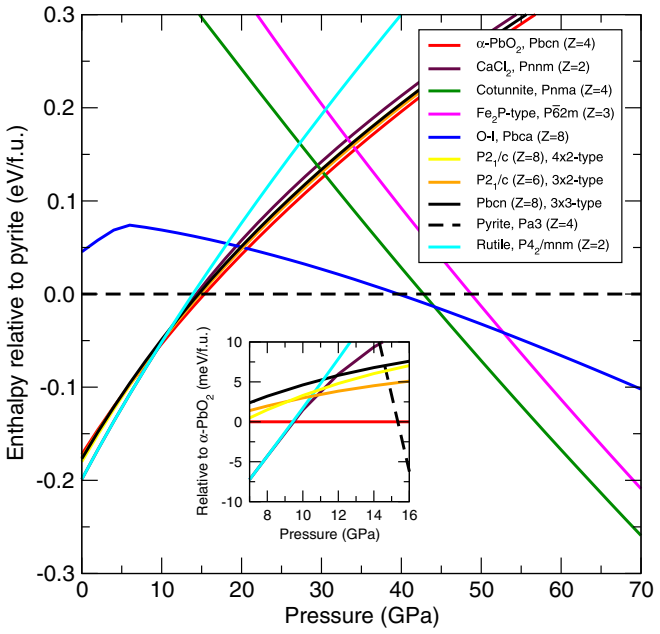

FIG. 4. Static-lattice enthalpies and results from structure searches on MgF_2 over the pressure range 0–70 GPa. The inset plot shows the small enthalpy differences between a few phases in the vicinity of 10 GPa. Enthalpies are shown relative to the pyrite (main figure) and α–PbO_2 (inset) phases.

MgF_2. In the present work, we find that the *Pbca* O-I "orthorhombic-I" structure, which has been reported experimentally for TiO_2 near 30 GPa [45], is also stable for MgF_2 between 39.6 and 44.1 GPa. This structure is depicted in Fig. 5. Experimental studies on MgF_2 have indeed reported an unidentified "Phase X" stable in the pressure range 49–53 GPa and at 1500–2500 K between the pyrite and cotunnite phases [46]. Our enthalpy calculations identify the O-I structure as the thermodynamically most likely candidate for Phase X, though the authors of Ref. [46] note some difficulty in indexing x-ray diffraction data on Phase X to an orthorhombic structure,

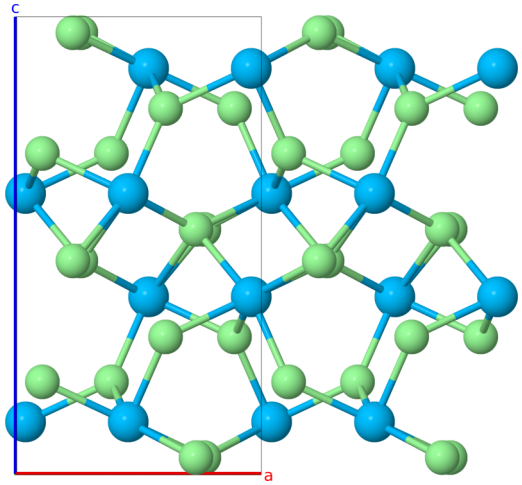

FIG. 5. $2 \times 1 \times 1$ slab of MgF_2 in the *Pbca* "orthorhombic-I" structure ($Z = 8$), which we predict to be stable between 39.6 and 44.1 GPa. This view looks down the *b* axis. Magnesium atoms in blue; fluorine atoms in green.

possibly due to a mixture of phases being present. We do not find any other energetically competitive structures near 50 GPa.

Silica and its stable polymorphs are of paramount importance in geophysics and planetary sciences. As well as a mineral in its own right, it is expected to be formed from the breakdown of postperovskite $MgSiO_3$ at terapascal pressures. SiO_2 follows a very similar set of phase transitions to MgF_2 with increasing pressure [47], with the Si coordination number rising from 6 in rutile at ambient pressures to a predicted 10 in an $I4/mmm$ structure near 10 TPa [48]. As pointed out by previous authors, several features of high pressure silica can readily be modeled in MgF_2, but at much lower pressures [10,46]. For example, the α–PbO_2 $\rightarrow$ pyrite transition in SiO_2, which our calculations find occurs at 217 GPa, takes place at a much lower pressure of 15.4 GPa in MgF_2. Near 690 GPa and for $T \gtrsim 1000$ K, a pyrite $\rightarrow$ cotunnite transition is also predicted for SiO_2 [49]; the analogous transition occurs at 44.1 GPa in MgF_2.

As mentioned in Sec. III B, Teter *et al.* [42] have introduced a class of SiO_2 polymorphs intermediate to $CaCl_2$ and α–PbO_2. At least one member of this class of polymorphs has been synthesized in SiO_2, the "3×2" type $P2_1/c$ structure [50]. The $P2_1/c$ ($Z = 6$), $P2_1/c$ ($Z = 8$), and $Pbcn$ ($Z = 8$) structures of BeF_2 depicted in Fig. 1(c) are members of this class, and also turn up in our MgF_2 searches (Fig. 4 and its inset). Our calculations show that these polymorphs are closest to stability near 10 GPa in MgF_2, compared to $\approx$100 GPa in SiO_2 suggesting that, as with other features of silica, they could be studied experimentally at much lower pressures in MgF_2.

Figure 3 shows the optical band gap in MgF_2 as a function of pressure. Like BeF_2, the optical gap is tunable with pressure, rising by about 0.04 eV/GPa over 0–70 GPa. We also provide the electronic DOS of the O-I structure as Supplemental Material [18].

V. CALCIUM DIFLUORIDE

CaF_2 crystallizes in the cubic $Fm\bar{3}m$ "fluorite" structure ($Z = 4$, α–CaF_2) under ambient conditions. The compound has a high-temperature phase above about 1400 K, known as β–CaF_2, and melts near 1700 K at low pressures [51]. A high-pressure modification above 8–10 GPa (γ–CaF_2) is also known, with CaF_2 taking on the orthorhombic *Pnma* cotunnite structure ($Z = 4$) [52].

The β phase has attracted considerable interest because it exhibits superionicity, with F^- ions as the diffusing species [53]. A number of other compounds in the same fluorite (or "antifluorite") variants of this structure, such as Li_2O, are also superionic conductors [54]. Such materials are of great technological interest, with applications in solid-state battery design. A recent study has shown that the superionic transition temperature in CaF_2 can be decreased through applied stress [55].

A. Results from structure searching

Our results from structure searching in CaF_2 are shown in Fig. 6. Unlike BeF_2 and MgF_2, we find that the potential energy surface for CaF_2 is relatively simple, with very few polymorphs for this compound over the pressure range 0–70 GPa. At the

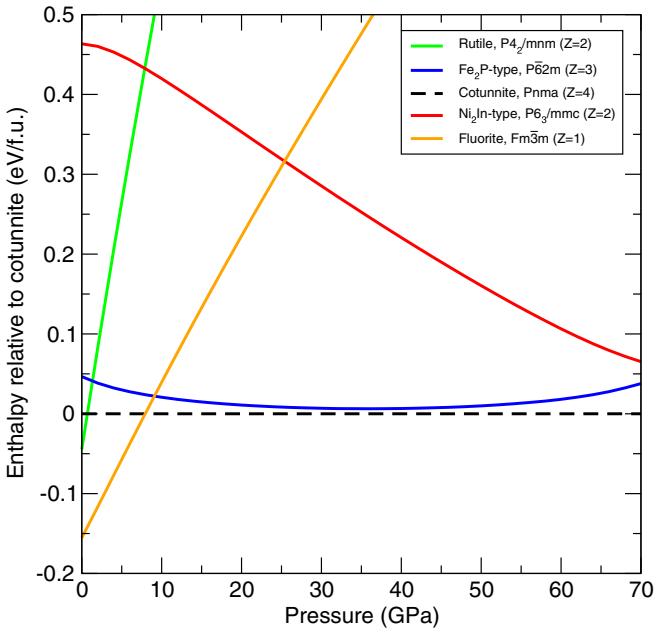

FIG. 6. Results from structure searches on CaF_2 over the pressure range 0–70 GPa: static-lattice enthalpies relative to the $Pnma$ (γ) CaF_2 phase.

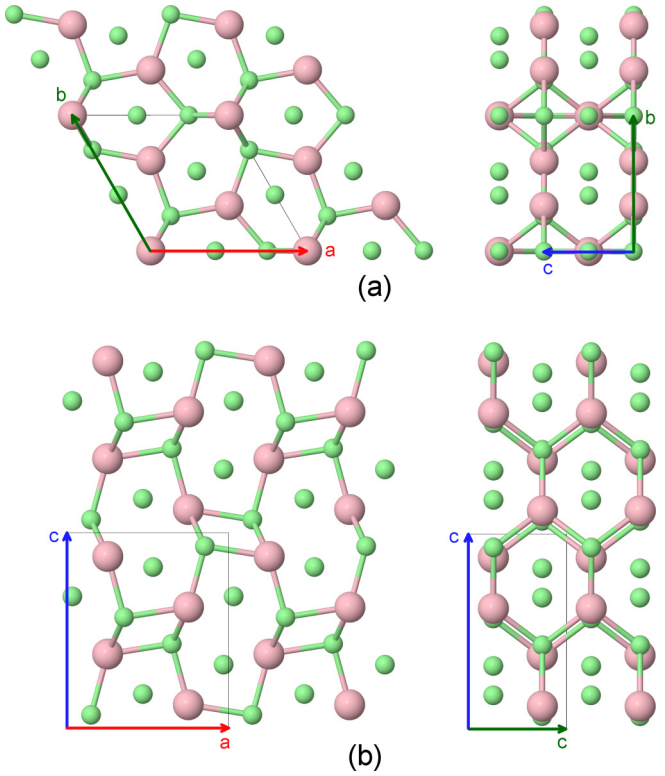

FIG. 7. $2 \times 2 \times 2$ slabs of (a) our predicted $P\bar{6}2m$ structure, and (b) the $Pnma$ structure (phase γ) of CaF_2. Calcium atoms are in red; fluorine atoms in green. In both (a) and (b), the right-hand view is obtained from the left-hand view by rotating the structure by 90° about an axis running vertically up the page.

static lattice level of theory, we identify only the sequence of stable phases and transitions:

$$\text{fluorite } (Fm\bar{3}m) \xrightarrow{7.9\ \text{GPa}} \text{cotunnite } (Pnma).$$

The calculated fluorite → cotunnite transition pressure here is in agreement with experimental results [52]. Experimental studies have also shown a transition from γ–CaF_2 to an Ni_2In-type structure in the pressure range 63–79 GPa with laser heating [56], consistent with the convergence of the red and black-dashed curves in Fig. 6.

Our results in Fig. 6 reveal a hexagonal phase for CaF_2 with $P\bar{6}2m$ symmetry which is close to stability, lying only 6 meV/CaF_2 higher in enthalpy than the γ phase near 36 GPa. The enthalpy curves for the $P\bar{6}2m$ and γ phases in Fig. 6 indicate that these two structures have very similar densities, with $P\bar{6}2m$ slightly denser at pressures below 36 GPa and becoming less dense than γ–CaF_2 at higher pressures. The $P\bar{6}2m$ phase has the Fe_2P structure, which has also been predicted for SiO_2 at very high pressures (>0.69 TPa) and low temperatures [49]. We show the γ and $P\bar{6}2m$ structures in Fig. 7.

B. Pressure-temperature phase diagram for CaF_2

The effects of nuclear zero-point motion and temperature are often important and affect the relative stability of crystal phases, particularly in cases where there are two or more structures lying very close in energy [57,58]. Given the small enthalpy difference between the $P\bar{6}2m$ and γ CaF_2 phases, we calculate the Gibbs free energy of these structures in the QHA as a function of pressure, as well as that of $Fm\bar{3}m$–CaF_2. Selecting the lowest Gibbs free energy structure at each temperature and pressure gives the phase diagram shown in Fig. 8. The solid-liquid phase boundary (dotted black line) in Fig. 8 is taken from the work of Cazorla *et al.* [59]. From this, we do indeed predict that the $P\bar{6}2m$–CaF_2 structure is stabilized by temperature, in the region $P \gtrsim 10$ GPa and $T \gtrsim 1500$ K. We remark here that the exact phase boundaries in Fig. 8 are subject to some uncertainty depending on the choice of equation of state used for the Gibbs free energy calculation. This uncertainty is particularly noticeable along the $Pnma$ (γ)-$P\bar{6}2m$ phase boundary.

Both the $Fm\bar{3}m$ and $P\bar{6}2m$ structures develop unstable phonon modes at sufficiently large volumes. For $Fm\bar{3}m$–CaF_2, these first occur at a static-lattice pressure between −7 and −6 GPa; for $P\bar{6}2m$ they first occur between 0 and 1 GPa. Cazorla *et al.* also report unstable phonon modes for $Fm\bar{3}m$–CaF_2 above 4.5 GPa [59]; however, we do not encounter any such instabilities in our calculations. We find no unstable phonon modes in γ–CaF_2. In Fig. 8, black dashed lines are used to divide the regions of stability for the $Fm\bar{3}m$ and $P\bar{6}2m$ phases in two. At temperatures below the lines, these phases have volumes corresponding to stable phonons, while above the lines they exhibit unstable phonon modes, and their Gibbs free energies are extrapolations of quasiharmonic results. Dotted lines separate regions where one or both phases have unstable phonon modes, with the exception of the solid-liquid boundary.

The calculated volume coefficient of thermal expansion, $\alpha(P,T)$, can be used to assess the validity of the QHA. Applying the criteria of Karki *et al.* [60] and Wentzcovitch

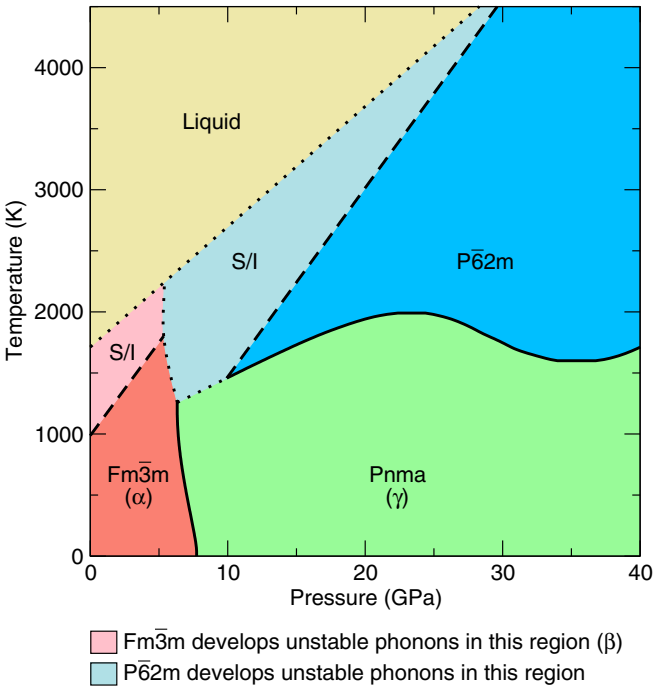

FIG. 8. Calculated quasiharmonic phase diagram of CaF_2. We find the known $Fm\bar{3}m$ (α) and $Pnma$ (γ) phases at low temperature, but our calculations indicate that a previously unreported phase of $P\bar{6}2m$ symmetry becomes stable at high temperature and pressure. "S/I" indicates the superionic region of the phase diagram, and dashed lines show boundaries due to unstable phonons at the quasiharmonic level.

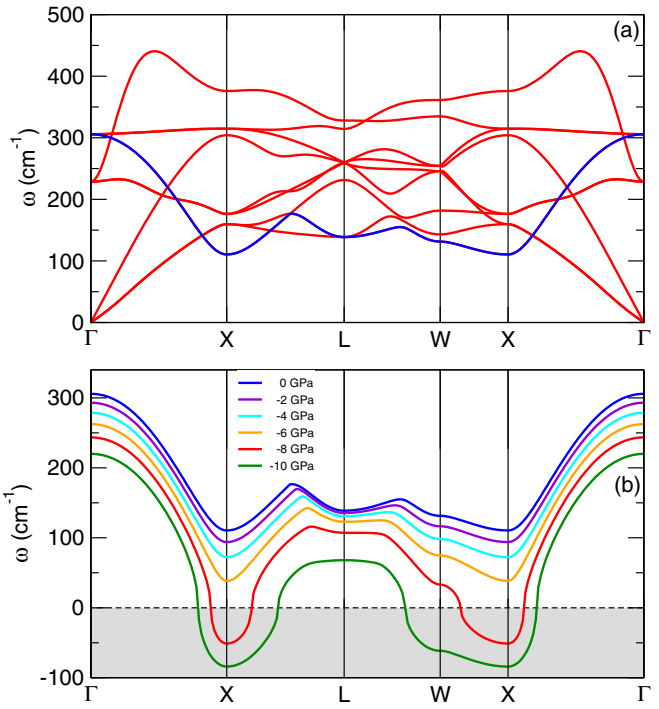

FIG. 9. Softening of phonon modes in the fluorite $Fm\bar{3}m$–CaF_2 structure. (a) Phonon dispersion curves of this structure at a static-lattice pressure of 0 GPa (cell volume 41.79 Å^3/f.u.). (b) The blue-colored mode in (a) as a function of decreasing static pressure, from 0 to −10 GPa. The mode softens and first develops imaginary phonon frequencies at X (shown as negative frequencies).

et al. [61], we expect the quasiharmonic approximation to be accurate for $T(\mathrm{K}) \leqslant 28P\ (\mathrm{GPa}) + 453$, with an uncertainty of about 100 K. The lower half of the α–γ phase boundary, and the γ–$P\bar{6}2m$ phase boundary near 40 GPa, are therefore expected to be accurate within the QHA. At higher temperatures, the QHA is expected to be less applicable as anharmonic effects become increasingly important. Further information on the calculation of $\alpha(P,T)$ and the validity of the QHA can be found as Supplemental Material [18].

C. Superionicity in CaF_2

The onset of superionicity in β–CaF_2 has been discussed in connection with the formation of unstable phonon modes in the fluorite CaF_2 structure [62]. Indeed, this is the criterion we have used in Fig. 8, where we label the region where $Fm\bar{3}m$–CaF_2 has unstable phonons as superionic ("S/I"), or β. By this criterion, the α–β transition is calculated to occur at ≈1000 K at 0 GPa, which is actually in rough agreement with the experimentally observed transition temperature of 1400 K, considering that the QHA should be inaccurate near unstable phonon modes. Figure 9(a) shows the phonon dispersion relations in $Fm\bar{3}m$–CaF_2 at a static-lattice pressure of 0 GPa, while Fig. 9(b) shows how unstable modes develop in this structure with increasing volume (decreasing static-lattice pressure). Unstable phonon modes are first encountered at the Brillouin zone X point. The corresponding atomic displacements in this unstable mode leave Ca^{2+} ions fixed, while F^- ions are displaced along the [100], [010], or [001] directions (referred to a conventional cubic cell for $Fm\bar{3}m$–CaF_2). The connection to superionicity is that these directions also correspond to easy directions for F^- ion diffusion in the fluorite structure, and are almost barrierless at volumes corresponding to unstable X phonons [63].

Figure 9(b) also shows that at even larger volumes, unstable phonon modes develop at the Brillouin zone W point and that the entire $W - X$ branch becomes soft. As is the case at X, the corresponding phonon modes involve only F^- ion displacements, though in different directions: at W, F^- ions displace along the [011] and [0-11] directions. This may explain the observed gradual onset of superionicity in the fluorite structure [64]: as volume increases, further low-energy diffusion pathways corresponding to unstable phonon modes are opened up in the lattice.

Figure 10 shows the phonon dispersion relations in $P\bar{6}2m$. With increasing volume, this structure first develops unstable phonon modes at the Brillouin zone K point, and the atomic displacements of Ca^{2+} and F^- ions in the corresponding mode are depicted in Fig. 11. This mode is similar to the unstable mode found in fluorite CaF_2 at X, in the sense that it involves displacements of F^- ions and a sublattice of Ca^{2+} ions which remain fixed. F^- ions move along the [120], [210], or [1-10] directions, and all displacements are confined to the ab plane only. The $P\bar{6}2m$ structure can be visualized as layerlike: in Fig. 11, all atoms that are linked by bonds belong to the same layer, and all "isolated" atoms belong to a different layer. We

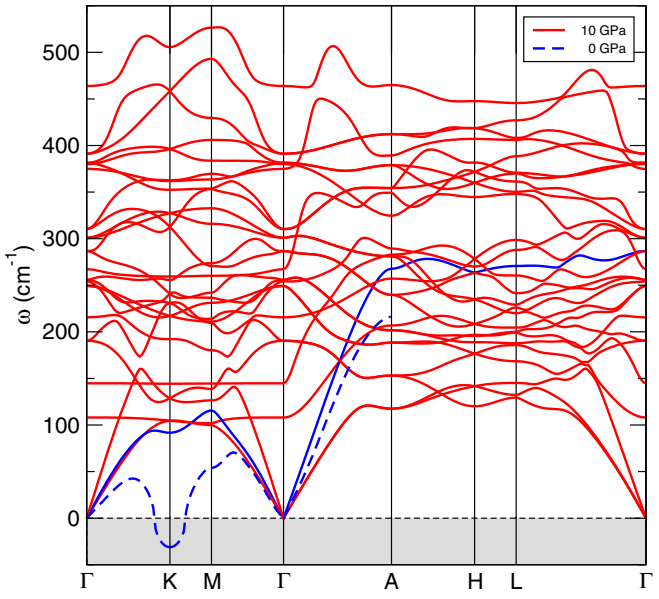

FIG. 10. Phonon dispersion curves for the proposed $P\bar{6}2m$–CaF_2 structure. This phase has stable phonons at a static pressure of 10 GPa (cell volume 34.45 Å^3/f.u.). The mode colored blue softens and becomes unstable at the Brillouin zone K point with decreasing pressure, as shown by the blue dashed curve. Only the portion from Γ to A is shown at 0 GPa.

find that Ca^{2+} ions in alternating layers remain fixed in the unstable phonon mode. By analogy with fluorite CaF_2, we propose that $P\bar{6}2m$–CaF_2 also undergoes a superionic phase transition accompanying this phonon mode, and we label the region where $P\bar{6}2m$ has unstable phonon modes in Fig. 8 as superionic ("S/I"). As is the case for the fluorite structure, it is possible that other compounds in the $P\bar{6}2m$ structure could also exhibit superionicity.

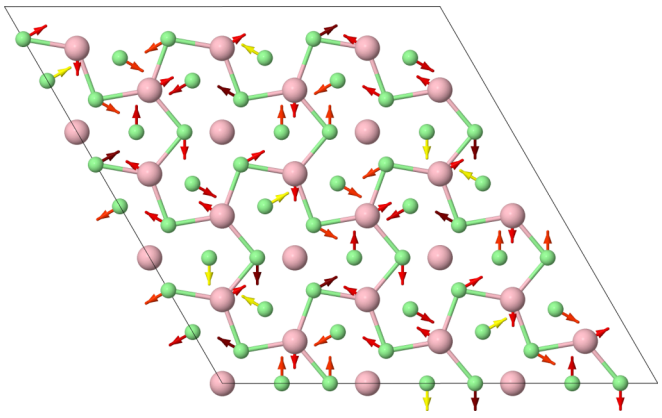

FIG. 11. Illustration of the unstable phonon mode in $P\bar{6}2m$–CaF_2 at the Brillouin zone K point, shown here at 0 GPa. A 3 × 3 × 1 slab of the structure is depicted, viewed along the c axis as in the left-hand panel of Fig. 7(a). Arrows indicate the direction of movement of atoms in this mode, and are color-coded according to their relative amplitudes: yellow for largest amplitude through to dark red for smallest amplitude. Calcium atoms are in red; fluorine atoms in green.

The pressure-temperature phase diagram of CaF_2 has recently been examined by Cazorla *et al.* [59,65]. In addition to the known α, β, and γ phases, the authors propose a high-temperature phase transition from γ to a new δ phase, which in turn is predicted to undergo a superionic transition at even higher temperatures, to a phase labeled ϵ–CaF_2. A $P2_1/c$ symmetry structure was proposed for the δ phase [59]; however, we find that this structure is close to $Pnma$ symmetry, and relaxing it using DFT gives the γ–CaF_2 structure. The phase diagram of Fig. 8 is in qualitative agreement with these results, where we identify the δ phase with our predicted $P\bar{6}2m$ structure, and the ϵ superionic phase with the region where $P\bar{6}2m$ has unstable phonon modes.

D. Optical band gaps in CaF_2

Our calculations show that optical band gaps in CaF_2 initially increase but then remain relatively constant over the pressure range 0–70 GPa (Fig. 3). We also show, using a dashed line Fig. 3, the calculated band gap for the $P\bar{6}2m$–CaF_2 phase, which begins to slowly decrease above 50 GPa. Semilocal DFT calculations using GGA functionals have also shown that this occurs for γ–CaF_2 above 70 GPa [66]. The optical band gap for γ–CaF_2 lies 0.9–1.2 eV above that of $P\bar{6}2m$–CaF_2 in the pressure range 10–70 GPa, suggesting that the formation of $P\bar{6}2m$–CaF_2 might be detectable in optical measurements. We also give the electronic DOS of the $P\bar{6}2m$ phase in the Supplemental Material [18].

Low temperature CaF_2 has been proposed as an internal pressure standard [52]. Our calculations of the band gap show that it remains a wide-gap insulator up to at least 70 GPa, and likely retains its superior optical properties up until high pressures.

VI. CONCLUSIONS

We have explored Be-, Mg-, and CaF_2 at pressures up to 70 GPa through DFT calculations and computational structure searching.

BeF_2 has a large number of polymorphs at ambient pressures, and shares many of these with SiO_2, such as α,β-quartz and α,β-cristobalite. Our searches show that BeF_2 has open-framework zeolite-like polymorphs, and that framework structures predicted in BeF_2 are energetically relevant to SiO_2, highlighting the utility of structure searching in model systems. At higher pressures, we find that BeF_2 is stable in the moganite structure between 11.6 and 30.1 GPa, and stable in the $CaCl_2$ structure between 30.1 and 57.5 GPa.

In MgF_2, we find that the $Pbca$-symmetry "O-I" TiO_2 structure is a stable intermediary between the pyrite and cotunnite MgF_2 phases, and is the lowest enthalpy MgF_2 structure between 39.6 and 44.1 GPa. A class of polymorphs for SiO_2 intermediate to the $CaCl_2$ and α–PbO_2 structures, which are relevant at Earth mantle pressures and are close to stability near 100 GPa in SiO_2, also occur in MgF_2 but at much lower pressures (≈10 GPa).

We find that the Fe_2P-type $P\bar{6}2m$-symmetry structure for CaF_2 lies close in enthalpy to the known γ–CaF_2 phase over the pressure range 0–70 GPa. Calculations using the QHA show that this structure is stabilized at high pressure and temperature

($P \gtrsim 10$ GPa and $T \gtrsim 1500$ K). The $P\bar{6}2m$ structure develops unstable phonon modes at high temperatures, which we propose is associated with a superionic transition in this structure. $P\bar{6}2m$–CaF_2 and its region of phonon instability are consistent with the recently proposed δ and ϵ CaF_2 phases.

Be-, Mg-, and CaF_2 are wide-gap insulators. Calculations using the HSE06 functional show that the band gaps in BeF_2 and MgF_2 are tunable with pressure, rising by 0.06 eV/GPa and 0.04 GPa over the pressure range 0–70 GPa. The optical band gaps in CaF_2 are instead relatively constant over this pressure range.

ACKNOWLEDGMENTS

R.J.N. acknowledges financial support from the Engineering and Physical Sciences Research Council (EPSRC) of the UK (Grant No. EP/J017639/1). C.J.P. acknowledges financial support from a Royal Society Wolfson research merit award. J.R.N., R.J.N., and C.J.P. acknowledge use of the Archer facilities of the UK's national high-performance computing service, for which access was obtained via the UKCP consortium (Grants No. EP/K013688/1 and No. EP/K014560/1). J.R.N. acknowledges the support of the Cambridge Commonwealth Trust.

[1] W. H. Dumbaugh and D. W. Morgan, Preliminary ultraviolet transmission data for beryllium fluoride glasses, J. Non-Cryst. Solids **38**, 211 (1980).

[2] R. T. Williams, D. J. Nagel, P. H. Klein, and M. J. Weber, Vacuum ultraviolet properties of beryllium fluoride glass, J. Appl. Phys. **52**, 6279 (1981).

[3] J. P. M. van der Meer and R. J. M. Konings. Thermal and physical properties of molten fluorides for nuclear applications, J. Nucl. Mater. **360**, 16 (2007).

[4] R. Appel and C. D. Dyer, and J. N. Lockwood, Design of a broadband UV-visible α-barium borate polarizer, Appl. Opt. **41**, 2470 (2002).

[5] M. Daimon and A. Masumura, High-accuracy measurements of the refractive index and its temperature coefficient of calcium fluoride in a wide wavelength range from 138 to 2326 nm, Appl. Opt. **41**, 5275 (2002).

[6] R. M. Hazen and L. W. Finger, Calcium fluoride as an internal pressure standard in high-pressure/high-temperature crystallography, J. Appl. Crystallogr. **14**, 234 (1981).

[7] B. Grocholski, S.-H. Shim, and V. B. Prakapenka, Stability, metastability, and elastic properties of a dense silica polymorph seifertite, J. Geophys. Res. **118**, 4745 (2013).

[8] F. Dachille and R. Roy, High-pressure region of the silica isotypes, Z. Kristallogr. **111**, 451 (1959).

[9] K. A. Walsh, *Beryllium Chemistry and Processing* (ASM International, Materials Park, OH, 2009), Sec. 8.3.2.

[10] J. Haines, J. M. Leger, F. Gorelli, D. D. Klug, J. S. Tse, and Z. Q. Li, X-ray diffraction and theoretical studies of the high-pressure structures and phase transitions in magnesium fluoride, Phys. Rev. B **64**, 134110 (2001).

[11] C. J. Pickard and R. J. Needs, *Ab initio* random structure searching, J. Phys.: Condens. Matter **23**, 053201 (2011).

[12] R. J. Needs and C. J. Pickard, Perspective: Role of structure prediction in materials discovery and design, APL Mater. **4**, 053210 (2016).

[13] L. Pauling, The principles determining the structure of complex ionic crystals. J. Am. Chem. Soc. **51**, 1010 (1929).

[14] C. J. Pickard and R. J. Needs, High-Pressure Phases of Silane, Phys. Rev. Lett. **97**, 045504 (2006).

[15] C. J. Pickard and R. J. Needs, Metallization of aluminum hydride at high pressures: A first-principles study, Phys. Rev. B **76**, 144114 (2007).

[16] Y. Li, L. Wang, H. Liu, Y. Zhang, J. Hao, C. J. Pickard, J. R. Nelson, R. J. Needs, W. Li, Y. Huang, I. Errea, M. Calandra, F. Mauri, and Y. Ma, Dissociation products and structures of solid H_2S at strong compression, Phys. Rev. B **93**, 020103(R) (2016).

[17] A. Dewaele, N. Worth, C. J. Pickard, R. J. Needs, S. Pascarelli, O. Mathon, M. Mezouar, and T. Irifune, Synthesis and stability of xenon oxides Xe_2O_5 and Xe_3O_2 under pressure, Nat. Chem. **8**, 784 (2016).

[18] See Supplemental Material at http://link.aps.org/supplemental/10.1103/PhysRevB.95.054118 for further details about the DFT and quasiharmonic phonon calculations in this study, a list of known AB_2 structures used alongside our AIRSS searches, and lattice parameters, atomic positions, and electronic/phonon DOS for structures reported in this study.

[19] S. J. Clark, M. D. Segall, C. J. Pickard, P. J. Hasnip, M. I. J. Probert, K. Refson, and M. C. Payne, First principles methods using CASTEP, Z. Kristallogr. **220**, 567 (2005).

[20] D. Vanderbilt, Soft self-consistent pseudopotentials in a generalized eigenvalue formalism, Phys. Rev. B **41**, 7892(R) (1990).

[21] J. P. Perdew, K. Burke, and M. Ernzerhof, Generalized Gradient Approximation Made Simple, Phys. Rev. Lett. **77**, 3865 (1996); **78**, 1396 (1997).

[22] B. B. Karki and R. M. Wentzcovitch, Vibrational and quasiharmonic thermal properties of CaO under pressure, Phys. Rev. B **68**, 224304 (2003).

[23] P. Carrier, R. Wentzcovitch, and J. Tsuchiya, First-principles prediction of crystal structures at high temperatures using the quasiharmonic approximation, Phys. Rev. B **76**, 064116 (2007).

[24] J. Heyd, G. E. Scuseria, and M. Ernzerhof, Hybrid functionals based on a screened Coulomb potential, J. Chem. Phys. **118**, 8207 (2003); **124**, 219906 (2006).

[25] The use of nonlocal functionals in CASTEP-8.0 necessitates the use of norm-conserving pseudopotentials.

[26] R. J. Nicholls, A. J. Morris, C. J. Pickard, and J. R. Yates, OptaDOS - a new tool for EELS calculations, J. Phys.: Conf. Ser. **371**, 012062 (2012).

[27] A. J. Morris, R. J. Nicholls, C. J. Pickard, and J. R. Yates, OptaDOS: A tool for obtaining density of states, core-level and optical spectra from electronic structure codes, Comput. Phys. Commun. **185**, 1477 (2014).

[28] J. R. Yates, X. Wang, D. Vanderbilt, and I. Souza, Spectral and Fermi Surface Properties from Wannier Interpolation, Phys. Rev. B **75**, 195121 (2007).

[29] A. F. Wright, A. N. Fitch, and A. C. Wright, The preparation and structure of the α- and β-quartz polymorphs of beryllium fluoride, J. Solid State Chem. **73**, 298 (1988).

[30] P. Ghalsasi and P. S. Ghalsasi, Single crystal x-ray structure of BeF_2: α-quartz, Inorg. Chem. **50**, 86 (2011).
[31] I. Jackson, Melting of the silica isotypes SiO_2, BeF_2, and GeO_2 at elevated pressures, Phys. Earth Planet. Int. **13**, 218 (1976).
[32] K. P. Driver, R. E. Cohen, Z. Wu, B. Militzer, P. López Ríos, M. D. Towler, R. J. Needs, and J. W. Wilkins, Quantum Monte Carlo computations of phase stability, equations of state, and elasticity of high-pressure silica, Proc. Natl. Acad. Sci. USA **107**, 9519 (2010).
[33] M. S. Rakitin, A. R. Oganov, H. Niu, M. M. D. Esfahani, X.-F. Zhou, G.-R. Qian, and V. L. Solozhenko, A novel phase of beryllium fluoride at high pressure, Phys. Chem. Chem. Phys. **17**, 26283 (2015).
[34] S. Coh and D. Vanderbilt, Structural stability and lattice dynamics of SiO_2 cristobalite, Phys. Rev. B **78**, 054117 (2008).
[35] F. H. Allen, G. Bergerhoff, and R. Sievers, *Crystallographic Databases* (International Union of Crystallography, Chester, England, 1987).
[36] Ch. Baerlocher and L. B. McCusker, Database of Zeolite Structures: http://www.iza-structure.org/databases/.
[37] M. B. Boisen, Jr., G. V. Gibbs, and M. S. T. Bukowinski, Framework silica structures generated using simulated annealing with a potential energy function based on an $H_6Si_2O_7$ molecule, Phys. Chem. Minerals **21**, 269 (1994).
[38] V. A. Blatov, A. P. Shevchenko, and D. M. Proserpio, Applied topological analysis of crystal structures with the program package ToposPro, Cryst. Growth Des. **14**, 3576 (2014).
[39] A. Černok, E. Bykova, T. B. Ballaran, H.-P. Liermann, M. Hanfland, and L. Dubrovinsky, High-pressure crystal chemistry of coesite-I and its transition to coesite-II, Z. Kristallogr. **229**, 761 (2014).
[40] A. Togo, F. Oba, and I. Tanaka, First-principles calculations of the ferroelastic transition between rutile-type and $CaCl_2$-type SiO_2 at high pressures, Phys. Rev. B **78**, 134106 (2008).
[41] F. Yu, M. Xu, M. Jiang, and J.-X. Sun, The phase transitions and electronic structures of crystalline BeF_2 under high-pressure: First-principle calculations, Solid State Commun. **169**, 14 (2013).
[42] D. M. Teter, R. J. Hemley, G. Kresse, and J. Hafner, High Pressure Polymorphism in Silica, Phys. Rev. Lett. **80**, 2145 (1998).
[43] H. Öztürk, C. Kürkçü, and C. Kürkçü. High-pressure structural phase transitions and intermediate phases of magnesium fluoride, J. Alloys Compd. **597**, 155 (2014).
[44] V. Kanchana, G. Vaitheeswaran, and M. Rajagopalan, High-pressure structural phase transitions in magnesium fluoride studied by electronic structure calculations, J. Alloys Compd. **352**, 60 (2003).
[45] N. A. Dubrovinskaia, L. S. Dubrovinsky, R. Ahuja, V. B. Prokopenko, V. Dmitriev, H.-P. Weber, J. M. Osorio-Guillen, and B. Johansson, Experimental and Theoretical Identification of a New High-Pressure TiO_2 Polymorph, Phys. Rev. Lett. **87**, 275501 (2001).
[46] B. Grocholski, S.-H. Shim, and V. B. Prakapenka, Stability of the $MgSiO_3$ analog $NaMgF_3$ and its implication for mantle structure in super-Earths, Geophys. Res. Lett. **37**, L14204 (2010).
[47] S. Wu, K. Umemoto, M. Ji, C.-Z. Wang, K.-M. Ho, and R. M. Wentzcovitch, Identification of post-pyrite phase transitions in SiO_2 by a genetic algorithm, Phys. Rev. B **83**, 184102 (2011).
[48] M. J. Lyle, C. J. Pickard, and R. J. Needs, Prediction of 10-fold coordinated TiO_2 and SiO_2 structures at multimegabar pressures, Proc. Natl. Acad. Sci. USA **112**, 6898 (2015).
[49] T. Tsuchiya and J. Tsuchiya, Prediction of a hexagonal SiO_2 phase affecting stabilities of $MgSiO_3$ and $CaSiO_3$ at multimegabar pressures, Proc. Natl. Acad. Sci. USA **108**, 1252 (2011).
[50] J. Haines, J. M. Léger, F. Gorelli, and M. Hanfland, Crystalline Post-Quartz Phase in Silica at High Pressure, Phys. Rev. Lett. **87**, 155503 (2001).
[51] P. W. Mirwald and G. C. Kennedy, The phase relations of calcium fluoride (fluorite) to 60 kbars and 1800 °C, J. Phys. Chem. Solids **39**, 859 (1978).
[52] L. Gerward, J. S. Olsen, S. Steenstrup, M. Malinowski, S. Åsbrink, and A. Waskowska, X-ray diffraction investigations of CaF_2 at high pressure, J. Appl. Crystallgr. **25**, 578 (1992).
[53] M. J. Gillan, Collective dynamics in super-ionic CaF_2: I. Simulation compared with neutron-scattering experiment, J. Phys. C: Solid State Phys. **19**, 3391 (1986).
[54] A. D. Mulliner, P. C. Aeberhard, P. D. Battle, W. I. F. David, and K. Refson, Diffusion in Li_2O studied by non-equilibrium molecular dynamics for $873 < T/K < 1603$, Phys. Chem. Chem. Phys. **17**, 21470 (2015).
[55] C. Cazorla and D. Errandonea, Giant mechanocaloric effects in fluorite-structured superionic materials, Nano Lett. **16**, 3124 (2016).
[56] S. M. Dorfman, F. Jiang, Z. Mao, A. Kubo, Y. Meng, V. B. Prakapenka, and T. S. Duffy. Phase transitions and equations of state of alkaline earth fluorides CaF_2, SrF_2, and BaF_2 to Mbar pressures, Phys. Rev. B **81**, 174121 (2010).
[57] J. R. Nelson, R. J. Needs, and C. J. Pickard, Calcium peroxide from ambient to high pressures, Phys. Chem. Chem. Phys. **17**, 6889 (2015).
[58] C. J. Pickard, M. Martinez-Canales, and R. J. Needs, Density functional theory study of phase IV of solid hydrogen, Phys. Rev. B **85**, 214114 (2012); **86**, 059902(E) (2012).
[59] C. Cazorla and D. Errandonea, Superionicity and Polymorphism in Calcium Fluoride at High Pressure, Phys. Rev. Lett. **113**, 235902 (2014).
[60] B. B. Karki, R. M. Wentzcovitch, S. de Gironcoli, and S. Baroni, First principles thermoelasticity of $MgSiO_3$-perovskite: consequences for the inferred properties of the lower mantle, Geophys. Res. Lett. **28**, 2699 (2001).
[61] R. M. Wentzcovitch, B. B. Karki, M. Cococcioni, and S. de Gironcoli, Thermoelastic Properties of $MgSiO_3$-Perovskite: Insights on the Nature of the Earth's Lower Mantle, Phys. Rev. Lett. **92**, 018501 (2004).
[62] L. L. Boyer, Nature of Melting and Superionicity in Alkali and Alkaline-Earth Halides, Phys. Rev. Lett. **45**, 1858 (1980).

[63] M. K. Gupta, P. Goel, R. Mittal, N. Choudhury, and S. L. Chaplot, Phonon instability and mechanism of superionic conduction in Li_2O, Phys. Rev. B **85**, 184304 (2012).

[64] S. Hull, Superionics: crystal structures and conduction processes, Rep. Prog. Phys. **67**, 1233 (2004).

[65] C. Cazorla and D. Errandonea. High-pressure, high-temperature phase diagram of calcium fluoride from classical atomistic simulations, J. Phys. Chem. C **117**, 11292 (2013).

[66] H. Shi, W. Luo, B. Johansson, and R. Ahujia, Electronic and elastic properties of CaF_2 under high pressure from ab initio calculations, J. Phys.: Condens. Matter **21**, 415501 (2009).